Fast electron transport and induced heating in solid targets from rear-side interferometry imaging

G. Malka,[1,*] Ph. Nicolaï,[2,†] E. Brambrink,[3] J. J. Santos,[2] M. M. Aléonard,[1] K. Amthor,[4] P. Audebert,[3] J. Breil,[2] G. Claverie,[1] M. Gerbaux,[1] F. Gobet,[1] F. Hannachi,[1] V. Méot,[5] P. Morel,[5] J. N. Scheurer,[1] M. Tarisien,[1] and V. Tikhonchuk[2]

[1]*Université Bordeaux 1, CNRS/IN2P3, Centre d'Etudes Nucléaires de Bordeaux Gradignan (CENBG), Chemin du Solarium, 33175 Gradignan, France*

[2]*Centre Lasers Intenses et Applications (CELIA), Université Bordeaux 1-CEA-CNRS, 33405 Talence cedex, France*

[3]*Laboratoire pour l'Utilisation de Lasers Intenses (LULI), CNRS-CEA-Ecole Polytechnique-Université Pierre et Marie Curie, 91128 Palaiseau Cedex, France*

[4]*Institut fur Optik und Quantenelektronik, Friedrich-Schiller-Universitat, Jena, Germany and*

[5]*Commissariat à l'Energie Atomique, Service de Physique Nucléaire, 91680 Bruyères-Le-Châtel, France*

(Received 18 July 2007; published 25 February 2008)

Fast adiabatic plasma heating of a thin solid target irradiated by a high intensity laser has been observed by an optical fast interferometry diagnostic. It is driven by the hot electron current induced by the laser plasma interaction at the front side of the target. Radial and longitudinal temperature profiles are calculated to reproduce the observed rear-side plasma expansion. The main parameters of the suprathermal electrons (number, temperature, and divergence) have been deduced from these observations.

DOI: 10.1103/PhysRevE.77.026408 PACS number(s): 52.50.Jm, 52.25.Xz

I. INTRODUCTION

High-energy particles, such as electrons, protons, ions, neutrons, x and γ rays, generated by ultraintense laser pulses are of great interest for radiography [1], fast ignition of fusion reactions [2], medicine [3], and nuclear physics [4]. Since the 100 TW class laser systems using the chirped pulse amplification (CPA) technique [5] became available, the number and energy of these particles have considerably increased. In particular, protons and other ions species can be accelerated to MeV energies at the rear side of a thin, laser irradiated aluminum foil, in the electric sheath layer created by relativistic electrons [1]. To control the characteristics of ion acceleration, one needs a good understanding of the fast electron transport in the solid target including their spatial distribution and energy deposition. These electrons generated at high laser intensities, above 10^{18} W/cm^2, have a mean energy of a few hundred keV or more. They are weakly collisional and their mean free path usually exceeds the target size. Because of their high current density (above 10^{12} A/cm^2), these electrons can propagate into the target, only in the presence of a return current of thermal electrons. The electric field dragging thermal electrons may be as large as 10 MV/cm. It inhibits the fast electron transport [6] especially in dielectric targets, where there are initially no free electrons. Effectively, the electric field amplitude is determined by the target conductivity. It modifies significantly the fast electron distributions and provides a dissipation of the electron beam energy in the target.

Various diagnostics have been used to characterize the electron energy spectrum and angular distribution. Theoretical [7] and experimental results [8] have shown that the ohmic heating by the return current leads to a high target temperature. Based on the detection of optical emission at the target rear side or x-ray K-α radiation emitted from a layer buried inside the target, measurements indicate a temperature in the range of a few eV to a few hundred eV at 10–10 μm depth into the targets. These diagnostics are rather complicated and indirect; for interpretation they require intensive numerical simulations [8,9]. So, it is interesting to validate these measurements through other diagnostics based on different physical processes.

In this paper, we report on the characterization of the aluminum plasma created by the fast electrons at the rear side of a solid target irradiated by an ultraintense laser beam. The density profile of the plasma expansion has been determined from interferometric measurements using an auxiliary probe beam at the second harmonic of the main laser pulse. By varying the time delay of the probe beam, we have measured the velocity and the shape of the expanding plasma for various target thicknesses. The measurement of the expansion velocity allows us to reconstruct the initial and the final temperature distributions of the aluminum plasma and so the spatial distribution of energy deposited by the fast electrons. A similar diagnostic has been recently used for a better characterization of the energy transport pattern in solid targets [10]. In the present work, we follow the same approach by considering the profiles of the plasmas generated from the targets. Moreover, combining these plasma expansion measurements, a two-dimensional (2D) hydrodynamic code, and a specific analytic model [11] of fast electron transport, we can evaluate the main parameters of the current of fast electrons crossing the target (energy of these fast electrons, their divergence, their radial energy distribution, and the total energy deposition versus the target thickness).

The experimental setup and the qualitative analysis of the experimental results are presented in Sec. II. The numerical simulations and the plasma expansion interpretations are described in Sec. III. The main results are summarized and discussed in Sec. IV.

*malka@cenbg.in2p3.fr

†nicolai@celia.u-bordeaux1.fr

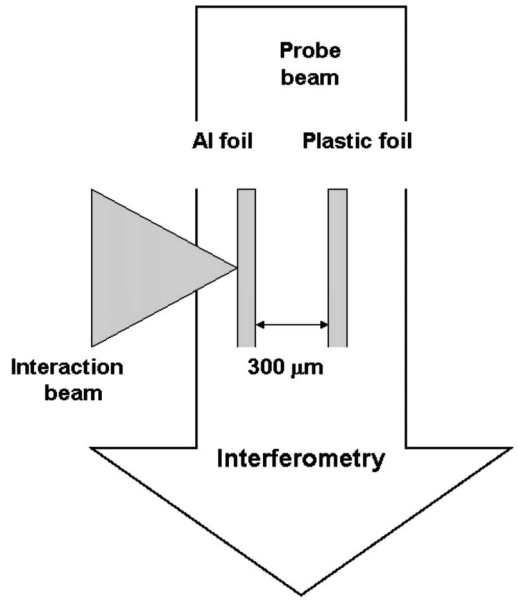

FIG. 1. Experimental setup. The plasma expansion is measured using a fast and time resolved interferometric diagnostic.

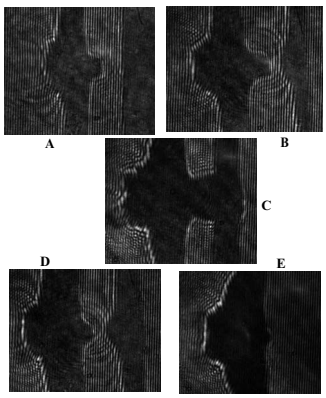

FIG. 2. Experimental expansions at instant of (a) 240, (b) 480, and (c) 830 ps after the UHI laser pulse for the 9 μm thickness Al target and at instant of 480 and 440 ps for the (d) 20 and (e) 50 μm thickness targets. The laser beam arrives from left. In (e), there is no plastic foil. In (c), at later time, the two plasmas generated by particles collide with fast speed. The interfringe distance is 10 μm and the full size of each image is 500×600 μm.

II. EXPERIMENTAL RESULTS

A. Experimental setup and measurements

The experiment was performed at the 100 TW CPA laser system at the LULI (Laboratoire pour l'Utilization de Lasers Intenses). The laser beam with an energy of 20 J in 500 fs and a 1.064 μm wavelength was focused with an f/4 off-axis parabola onto an aluminum foil providing peak intensities of $(2-3)\times10^{19}$ W/cm^2. The focal spot was 7 μm (FWHM). A long prepulse (1.5 ns), with an intensity contrast ratio of 10^{-6}, creates a preplasma in front of the target. The target thickness was varied from 5 to 50 μm. The target is a long thin foil with a 2 mm transverse width. A thin plastic foil was set 300 μm behind the aluminum target. The density profiles of the expanding plasmas were probed by a sub-ps, frequency doubled (532 nm) laser pulse, propagating parallel to the target surface (Fig. 1). This beam was used to obtain an interference pattern combining a 2° Wollaston crystal with two polarizers.

Targets were imaged with a magnification of 10, leading to a spatial resolution better than 5 μm. The delay between the probe beam and the main laser pulse was measured with a streak camera, providing a precision of ±10 ps. By varying this delay, the plasma temporal evolution was studied up to 1 ns. The interferograms were unfolded with the Abel inversion to calculate the transverse and the longitudinal density profiles from the fringe shifts assuming an axial symmetry. Typical interferograms are shown in Fig. 2. The interfringe is 10 μm.

At the front of the target, one observes an aluminum plasma created by the intense beam and its prepulse. At the rear side of the target, one observes another aluminum plasma. This plasma cannot be produced directly by the laser beam, since 9 μm Al is opaque to the laser light and is too thick to be fully ablated by the prepulse beam (see Sec. III C). Figures 2(a)–2(c) show, for 9 μm thick Al targets, the plasma expansion at 240, 480, and 830 ps after the intense pulse. The plasma shapes are quite different at the target front and rear sides. At later times [Fig. 2(b)], another plasma is created on the second plastic foil; this plasma is generated by fast particles, as was already discussed in Ref. [12]. Much later [Fig. 2(c)], these two plasmas generated by fast particles collide with a velocity of a few hundreds km/s.

In the following, we consider only the rear-side expansion of the aluminum target as it provides information on the electron beam instead of the direct effect of the laser pulse. At the back side of this target, the interferograms have a distinct rectangular shape. Figures 2(d) and 2(e) present the plasma plume shape for the 20 and 50 μm thick targets, respectively, at 480 and 440 ps after the intense pulse. The square shape, clearly seen for the 9 μm target at equivalent time delay [Fig. 2(a)], still appears for the 20 μm target, though less distinct. However, it disappears for the thickest target, 50 μm, and the expansion rate becomes smaller and more spherical. Other density profiles obtained at different time delays and for different target thicknesses confirm these observations. One of the main limitations in this measurement is due to the target width of 2 mm in the transverse direction (parallel to the probe beam) which introduced a large shadow of around 70 μm in the interferogram pattern. It gives a large uncertainty on the initial position of the back side of the target. Nevertheless, the large target width prevents current from flowing around the edges.

Figure 3 shows an on-axis longitudinal electron density profile of the plasma plume at the rear side of the 9 μm target, using Abel inversion. The plasma gradient scale length is very short, less than 20 μm, and it does not exceed this value during at least the first 800 ps. This is also true for other target thicknesses. Since the gradient scale length is of the order of the interfringe distance, the uncertainty on this value is quite large (50%).

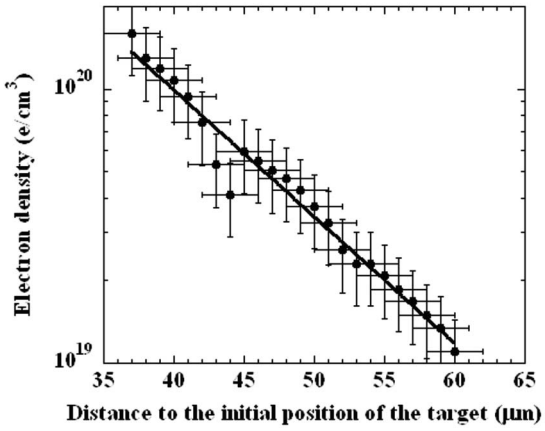

FIG. 3. Experimental electron density profile along the longitudinal axis (perpendicular to the target surface) at 173 ps after the UHI laser pulse for the 9 μm thick target.

B. Qualitative analysis

The summary of the data extracted from the interferograms is shown in Fig. 4. It presents the position of plasma electron density $\sim 10^{20}$ cm^{-3} as a function of the time elapsed from the main laser pulse for three target thicknesses. We see that the plasma expands with an almost constant velocity. The expansion velocity is found to be equal approximately to 170 ± 25, 95 ± 25, and 55 ± 25 km/s for the 9, 20, and 50 μm target thicknesses, respectively (Fig. 5). We calculate the initial temperature of the plasma assuming an adiabatic expansion and using the ideal gas approximation. Moreover, one can assume that the electron and ion temperatures are equal since the time for temperature equilibration in solid aluminum is ~ 2 ps [13]. We consider only aluminum in our calculation, we neglect the contribution of the very thin layer of contaminants (H, C, O) on the hydrodynamic simulations of the plasma expansion. Thus the specific internal energy can be written as $e=(Z+1)T/(\gamma-1)m_i$,

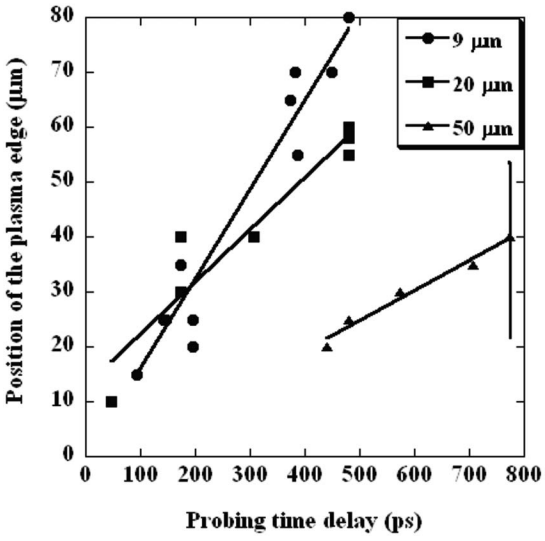

FIG. 4. Dependence of the plasma axial position vs the time for three target thicknesses for the electron density of 10^{20} cm^{-3}.

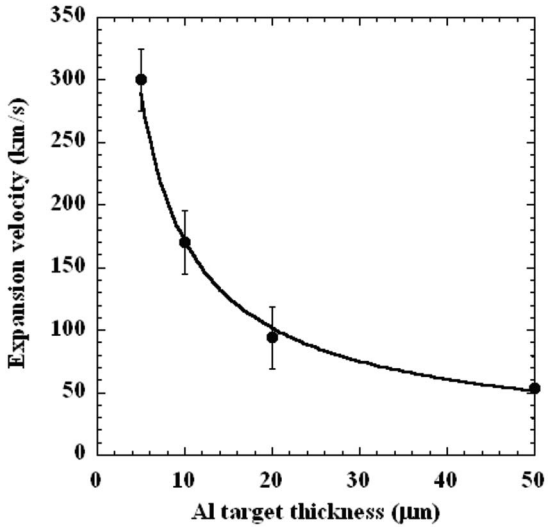

FIG. 5. Expansion velocity vs the target thickness.

where Z and m_i are the ion charge and mass, T is the temperature, and γ the polytrophic index. The sound speed is given by $C_s=\sqrt{\gamma P/\rho}$, where ρ is the density and $P=(\gamma-1)\rho e$ is the pressure. According to Ref. [14], a rarefaction front moves from the rear side inward with the sound velocity. The plasma front moves outward with the velocity $2C_s/(\gamma-1)$. Using the experimentally measured velocities and $\gamma=5/3$, one obtains $(Z+1)T=540$, 170, and 60 eV for the 9, 20, and 50 μm target thicknesses, respectively. Within this energy range, we calculate that the ion charge Z varies between 6 and 2.5 [15]. Under these conditions, we conclude that the expected initial Al plasma temperature should vary from 90 to 15 eV, at the targets rear side, as the target thickness increases from 9 to 50 μm. These analytic results are confirmed by more accurate numerical simulations performed with a 1D and 2D hydrodynamic code. They allow us to reduce the number of simulations required to reproduce the experimental expansion.

Important information that can be extracted from the interferometric images concern the plasma radial expansion. Figure 6 shows the diameter of the expanding plasma versus time. For all shots, except at early times for the thinnest target, the diameter of the plasma plume is close to 100 μm. It implies that the plasma expands axially without noticeable radial spreading. This can be explained by the fact that the pressure inside the plume decreases very quickly and it is not sufficient to push the matter radially. Therefore, the plasma motion has been initiated during the first 100 ps of its expansion. The second comment concerns the radial spreading of the fast electrons during their propagation through the target. Some observations [10,11] indicate that the angular divergence of the fast electrons may reach a few tens of degrees. That would imply that the plasma plume initial diameter increases with the target thickness. This fact is inconsistent with our experimental results showing approximately the same width for all target thicknesses. We will address this issue in the next section. Our 2D hydrodynamic code allows us to reconcile various results and to reconstruct the axial and radial shapes of the energy deposition in the targets.

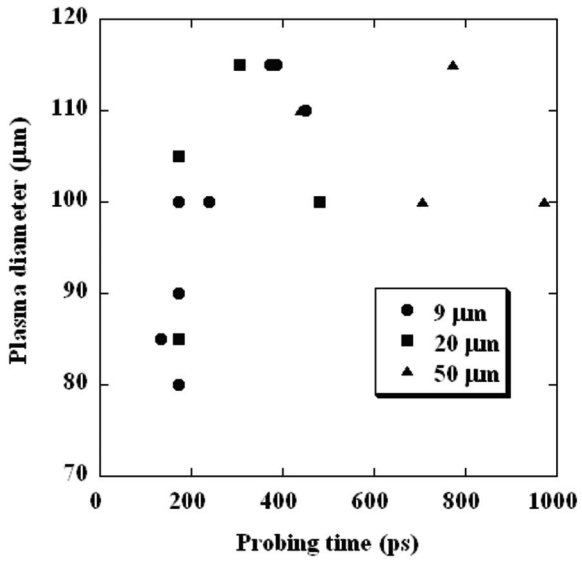

FIG. 6. Dependence of the diameter of expanding plasma on time for three target thicknesses.

III. INTERPRETATION OF EXPERIMENTAL RESULTS

The simulations of the plasma dynamics were performed with the laser-plasma interaction hydrodynamic code CHIC [16]. This code is currently used to simulate laser experiments [17]. The code includes two-dimensional axially symmetric hydrodynamics, ion and classical or nonlocal electron heat conduction, thermal coupling of electrons and ions, and detailed radiation transport. The arbitrary Lagrangian-Eulerian (ALE) method [18] is implemented to improve the geometrical quality of the grid elements. The ionization and the opacity data are tabulated assuming a local thermodynamic equilibrium (LTE) or a non-LTE depending on the plasma parameters. The equations of state implemented in the code (QEOS) are described in Ref. [15]. The laser propagation, refraction, and collisional absorption are treated by a ray tracing algorithm. A resistive MHD package accounting for the azimuthal magnetic fields generated by the thermal sources (crossed gradients of the density and the temperature) is also included.

A. Expansion velocities and plasma temperatures

The aim of the simulations was to find out the target temperature distribution, at initial time, created by the fast and return current heating. Since the hydrodynamic plasma motion is established in the scale of tens of ps, longer than the electron-ion equilibration time in solid aluminum, we assume that the plasma is in thermal equilibrium. We suppose that the laser prepulse did not modify strongly the target. This will be justified in Sec. III C. So the density of the plasma was assumed to be homogeneous and equal to the density of Al at normal conditions: 2.7 g cm^{-3}. The result of the initial on-axis temperature leading to the experimental expansion does not require 2D simulations. 1D hydrodynamic simulations confirm the previous analytic results (Sec. II B): 70 ± 10, 50 ± 10, and 20 ± 10 eV at the rear side for the 9, 20, and 50 μm target thicknesses, respectively. These values are in agreement with previous results obtained in similar conditions [8]. The variation of the rear side initial temperature with the target thickness leads us to suppose that the temperature is nonuniform across the target: the front side is hotter and the rear side is colder. Using average temperature data for three target thicknesses, one can find an analytic function describing the dependence of the initial on-axis temperature on the target thickness. Figure 7 shows two possible fits in the range of thicknesses 10–50 μm. Such a profile with a hotter zone at the front side of the target will provide a rear face expansion in agreement with the observations (delayed in time), as we will show in the next paragraph. We will use in what follows the initial temperature exponential profile: $T_e(z)=T_0e^{-z/z_0}$, where $z_0=30$ μm is a characteristic length and $T_0=95$ eV is the front face temperature.

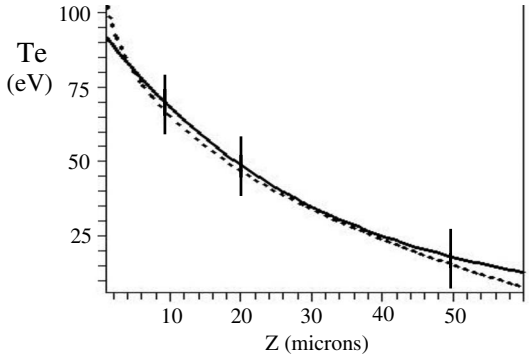

FIG. 7. On-axis initial temperature variation inside the target. Two analytical fits are shown: $T_e(z)=95e^{-z/30}$ (solid line) and $T_e(z)=-32.5z^{1/3}+135$ (dotted line).

B. Radial distribution of plasma temperature

One of the important experimental observations is related to the radial shape of the expanding plasma. As shown in the experiment (Fig. 2), for a thin target, the plasma has a square shape whereas for thicker targets, the plume shape becomes more spherical. That suggests that the temperature profile has a flat top shape near the target front side and it becomes smoother as one moves deeper inside. Consequently, the pressure inside the plasma decreases with the radius and so does the plasma expansion velocity. Therefore, one can explain the observed plasma expansion shape by adjusting the 2D profile of the initial temperature. Figure 8 shows the calculated plasma distribution after 300 ps, for two initial 2D temperature distributions. There is one-to-one correspondence between the temperature profile and the shape of the expanding plasma. Experimental data indicate that the target heating by the fast and return currents depends strongly on the distance from the front side. The energy deposition, which is correlated with the electron beam shape, seems to be flat with sharp edges close to the front side. Deeper in the target, the beam spreads laterally and the edges become smoother. We have interpolated the initial temperature profile with a radial (r) and a axial (z) dependence:

$$T_e(z,r) = T_0e^{-z/30} \quad \text{if} \quad r < r_c,$$

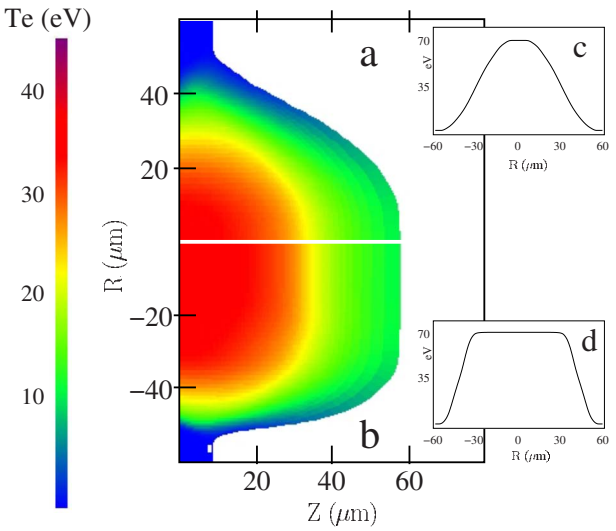

FIG. 8. (Color online) 2D plasma distributions 300 ps after the CPA pulse for two different initial temperature distributions. Panel (c) [(d)] shows the radial initial temperature distribution producing expansion (a) [(b)]. The target thickness is 9 μm and the axial temperature is shown in Fig. 7.

$$T_e(z,r) = T_0 e^{-z/30} \cos^2[(\pi/2)(r - r_c)/(r_e - r_c)] \quad \text{if} \quad r_c \leq r < r_e,$$

$$T_e(z,r) = 0 \quad \text{if} \quad r \geq r_e,$$

where $r_c(z) = 17 - 0.26z$ is the core radius and $r_e(z) = 45 + 0.58z$ is the edge radius. All lengths are in microns. This is an empiric formula which gives the best fit to the observed profiles of the plasma plume. Figure 9 presents this 2D initial temperature profile. The angular divergence and the edge smoothing effects can be better seen in line outs in Fig. 9(b). By comparing the dotted line giving the rear-side radial shape normalized to the front side value, one sees that, at half maximum, the radius increases by 10 μm whereas, at the foot, the radius increases by 30 μm.

Figure 10 shows the resulting plasma density distribution 400 ps after the intense pulse for three target thicknesses. The velocities and the plasma plume shapes observed in the interferometry images are correctly reproduced and whatever the thickness, the plasma plume diameter is approximatively

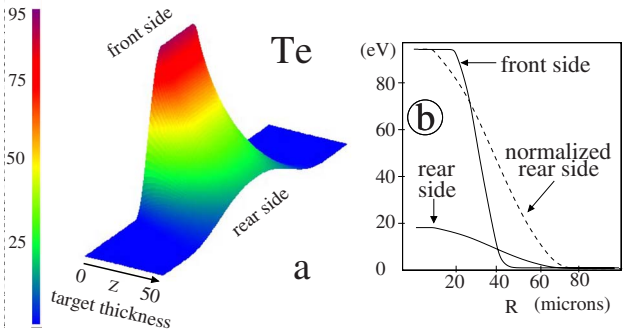

FIG. 9. (Color online) Initial 2D temperature distributions in the target. Panel (b) shows the radial initial temperature distribution (lineouts) at the front and rear sides.

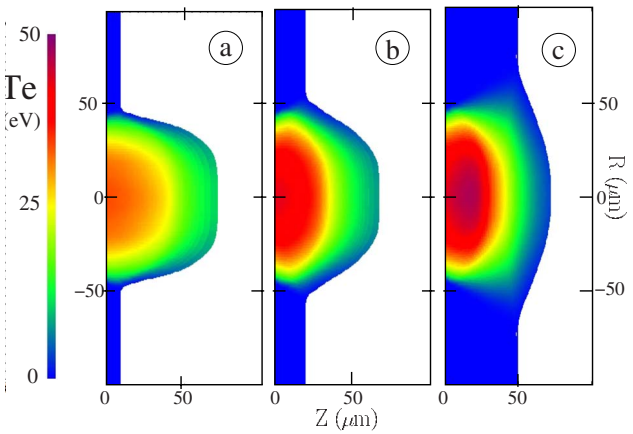

FIG. 10. (Color online) 2D temperature profiles of plasma expansion after 400 ps for (a) 9 μm, (b) 20 μm, and (c) 50 μm target thickness.

the same and close to 100 μm. This result agrees with experimental data shown in Fig. 6, completes the analysis, and leads to consistent results. Note that the temperature distribution deduced from the simulations characterizes a radial spreading of the fast electrons versus the penetration depth. Furthermore, one easily finds the total energy deposited in the targets as a function of their thicknesses. These temperature profiles correspond to energy deposit of 300, 550, and 900 mJ for the 9, 20, and 50 μm thicknesses, respectively. These values correspond to 1.5, 2.5, and 4.5% of the 20 J laser energy. In the next section, these results will be used to characterize the fast electron beam parameters.

C. Energy of fast electrons and prepulse influence

A kinetic model for the fast electron transport and induced heating has been developed recently and proved to describe the macroscopic characteristics: main divergence, spatial and temporal resolution of the energy deposition [11]. The model assumes a linear growth of the transverse size of the fast electron beam against target depth. It resolves in time the evolution of the background electron temperature considering both the resistive heating by the return current and the contribution of the fast electron collisions with the target electrons (in the Bethe-Bloch approximation). The model has the following four parameters. The fast electron source initial radius r_0 and the divergence half-angle θ. At a given depth z into the target, the radius of the incident beam is $r_b(z) = r_0 + z \tan \theta$. The laser energy conversion efficiency into fast electrons η and the temperature of the injected fast electron population T_h. We assume a relativistic Maxwellian energy distribution.

These parameters can be adjusted to produce in-depth longitudinal background electron temperature profiles $T_e(z)$ in agreement with the 1D hydrodynamic simulations results (see Fig. 7). According to the experimental laser intensity $(2-3) \times 10^{19}$ W cm^{-2}, the energy conversion efficiency should be within 20–30 % [19]. According to other experiments performed with the same laser system in similar configurations, T_h should be of a few hundred keV [11]. We

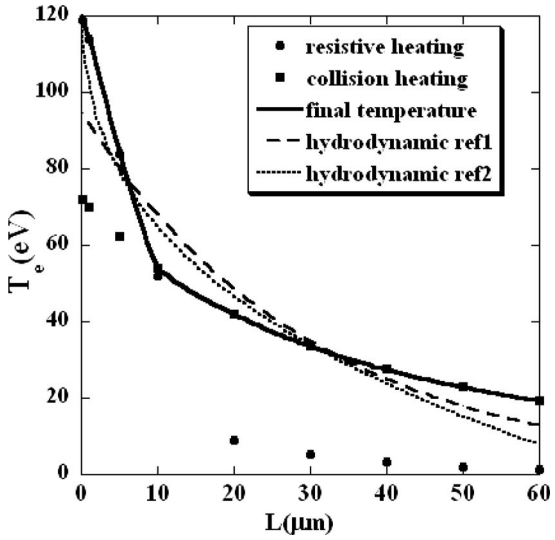

FIG. 11. Background electron temperature profile (solid line) with the model calculation for $r_0=23.5$ μm, $\theta=20°$, $\eta=25\%$, and $T_h=300$ keV for a target initially cold. Heating has a resistive origin (circle) for the first 10 μm and then, for deeper layers, collisions (square) become the dominant heating process. The on-axis initial temperature profiles from hydrodynamic simulations are in dotted lines (Fig. 7).

consider a solid (2.7 g cm^{-3}) and initially cold Al target.

Figure 11 shows the temperature profile obtained using the kinetic model calculation for $r_0=23.5$ μm, $\theta=20°$, $\eta=25\%$, and $T_h=300$ keV. Heating has a resistive origin for the first 10 μm and then, for deeper layers, because of the fast electrons divergence and consequent j_h diminution, the fast electron collisions become the dominant heating process. The temperature profile can be adjusted differently according to the approximate dependency $T_e(z)\propto(r_0+z\tan\theta)^{-4}$ for $z<10$ μm and $T_e(z)\propto(r_0+z\tan\theta)^{-2}$ for $z>10$ μm. A fair agreement between hydrodynamic simulations and the fast electron heating model can be found for values of $T_h=200-500$ keV, $r_0=17.5-25$ μm, and $\theta=10-20°$.

Now to be more realistic, one calculates, for the thinnest target, the laser prepulse influence. In the experiment, the prepulse duration is less than 1.5 ns and the intensity contrast ratio is estimated to 10^{-6}, which leads to a maximum intensity of 5×10^{12} W/cm^2. In Fig. 12, we present the density obtained under these conditions just before the intense pulse arrival (logarithmic scale). Although modified, the departure from a nonperturbed target remains small. The shock wave reaches the rear face at 1.2 ns, that is 300 ps before the main pulse arrival. However, for this laser intensity, the shock wave is not strong enough to induce large modifications [20]. The velocity of the rear side, due to the shock breakout, is less than 4 km/s. As shown in Fig. 12(b), the maximum density is about 3.6 g cm^{-3}, for a thickness close to 7 μm. Due to the wavelength used, the distance between the ablation front and the critical density, corrected by relativistic effects, is less than 0.5 μm. The level of background electron temperature reached on an ASE-perturbed 9 μm thickness is presented in Fig. 13. We see that because of the low-density preplasma, implying lower electrical conductivity [21,22], the background electron temperature reaches 800–900 eV over the first 100 nm depth, decreasing to values close to the unperturbed case (i.e., ~100 eV) after 1 μm. This rather hot front surface will not change the rear-side plasma expansion over the 700 ps following fast electron transport.

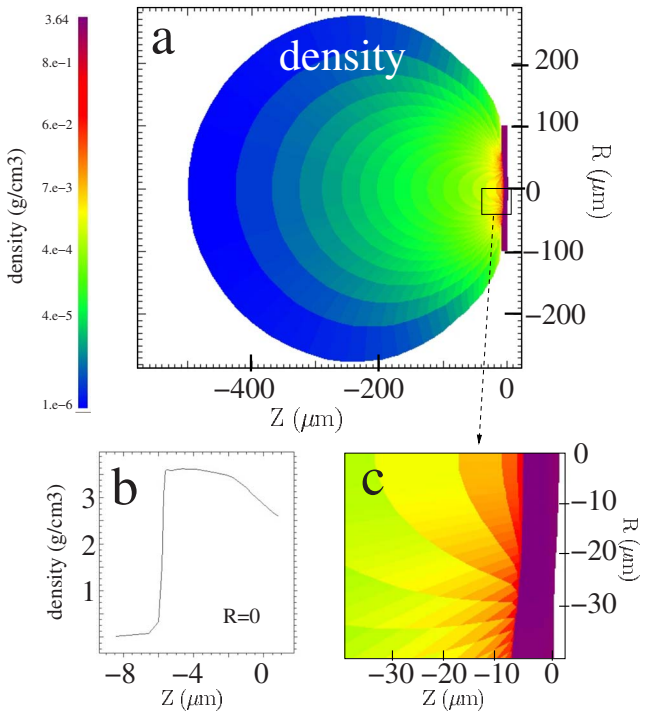

FIG. 12. (Color online) (a) Density distributions in the target at the end of the prepulse $t=1.5$ ns for the 9 μm target thickness. Panel (b) shows the axial ($R=0$) density distribution (lineout) and panel (c) is a zoom-in on the dense zone of the target.

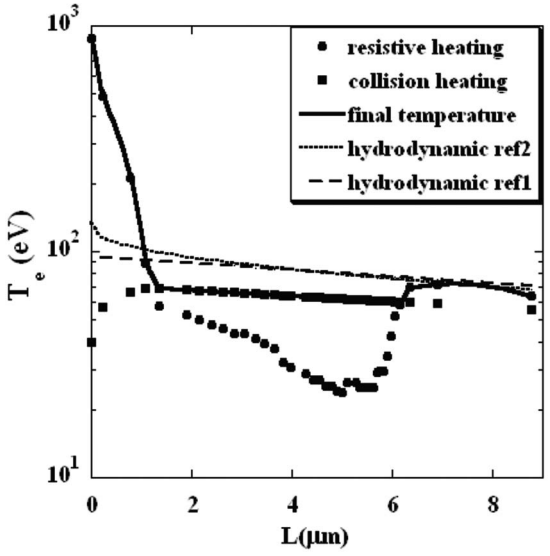

FIG. 13. Background electron temperature profile (solid line) with the model calculation. The same parameters of the fast electron beam of Fig. 11 have been used but including the effect of the preplasma induced by the pedestal of the laser beam. This effect can be neglected for targets thicker than 1 μm.

IV. CONCLUSION

We have studied a plasma expansion induced by fast electrons at the back side of aluminum targets. These fast electrons are accelerated by the interaction of an ultrahigh intensity laser pulse with the front side of the target. The fast electron beam yields target heating due to collisions and to the cold electron return current. After the laser pulse, the heated matter expands into vacuum while its density and velocity profiles vary with the temperature. We have recorded the density profiles of the expanding plasma using an interferometry diagnostic and the Abel inversion. We have demonstrated, from these experimental data, that the foils rear-side temperature reaches a few tens of eV. This temperature decreases as the target thickness increases. Moreover, from the 2D Abel deconvoluted density profiles and using a 2D hydrodynamic code, we have shown that one could obtain a detailed information on the in-depth energy deposition in plasma and consequently on the fast electron beam shape. To reproduce the experiment, we deduced the initial temperature profile giving access to the fast electron beam characteristics. This beam is well collimated with sharp edges at a few microns depth whereas, deeper in target, the beam widens and the edges become smoother. Modeling of the fast electron transport and energy deposition showed that the heating has a resistive origin for the first 10 μm and then, for deeper layers, because of the fast electron divergence, collisions become the dominant heating process. As verfied in another experiment [11], a fair agreement between hydrodynamic simulation results and model heating has been found for values $T_h=200-500$ keV, $r_0=17.5-25$ μm, and $\theta=10-20°$. For an univocal set of parameters, one should include additional diagnostics in the experiment (like rear-side visible imaging [11] or $K\alpha$ [23] imaging from fluorescent buried layers in the targets) to measure the fast electron divergence and penetration depth (function of T_h). The interferometry of expanding plasma combined with multidimensionnal hydrodynamic simulations could be a valuable diagnostic method for high intensity laser plasma interactions. Comparing our results with previous publications, we note that we did not find an evidence of the annular structure of the electron beam recently reported in Refs. [10,24]. This could be due, in the present work, to a lower laser intensity and the use of thicker targets. The laser intensity in Ref. [10] is about 5×10^{20} W cm^{-2} and the ring shape only appears for the 5 μm thick targets. The laser prepulse can play an important role in this case (thinner target and higher intensity). In summary, although characteristic time scales of the fast electron beam propagation through the target and of the resulting plasma expansion are completely different, relevant information can be obtained from the interferometry of the expanding plasma. Based on 2D hydrodynamic codes [16] and on simple physical models for the plasma expansion [14] and the fast electron induced heating [11], this approach is complementary to other diagnostics [8]. It confirms the results obtained with optical or x-ray emission. More generally, the propagation of other particles, protons, heavier ions, or photons in a target can be studied through the interferometry diagnostic coupled with others diagnostics and a hydrodynamic modeling of plasma expansion for time scales much longer than the duration of the interaction process.

ACKNOWLEDGMENTS

We acknowledge the fruitful comments of Arnaud Debayle and Benoit Chimier. This work is partially supported by the Region Aquitaine council and by the LULI laboratory in the frame of program LaserLab. We gratefully acknowledge the help of the LULI laser staff, of the CEA Bruyères-Le-Châtel target laboratory staff, and of the CENBG technical groups.

[1] A.J. Mackinnon *et al.*, Phys. Rev. Lett. **97**, 045001 (2006) and references therein.
[2] M. Tabak, J. Hammer, M. E. Glinsky, W. Kruer, S. Wilks, J. Woodworth, E. Campbell, M. Perry, and R. Mason, Phys. Plasmas **1**, 1626 (1994).
[3] V. Malka *et al.*, Med. Phys. **31**, 1587 (2004).
[4] K. Ledingham, P. McKenna, and R. Singhal, Science **300**, 1107 (2003); G. Malka *et al.*, Phys. Rev. E **66**, 066402 (2002).
[5] D. Strickland and G. Mourou, Opt. Commun. **56**, 219 (1985).
[6] F. Pisani *et al.*, Phys. Rev. E **62**, R5927 (2000).
[7] A. Bell, A. Robinson, M. Sherlock, R. Kingham, and W. Rozmus, Plasma Phys. Controlled Fusion **48**, R37 (2006).
[8] J. Koch *et al.*, Laser Part. Beams **16**, 225 (1998); E. Martinolli *et al.*, Phys. Rev. E **73**, 046402 (2006).
[9] L. Gremillet, G. Bonnaud, and F. Amiranoff, Phys. Plasmas **9**, 941 (2002).
[10] K. L. Lancaster, J. S. Green, D. S. Hey, K. U. Akli, J. R. Davies, R. J. Clarke, R. R. Freeman, H. Habara, M. H. Key, R. Kodama, K. Krushelnick, C. D. Murphy, M. Nakatsutsumi, P. Simpson, R. Stephens, C. Stoeckl, T. Yabuuchi, M. Zepf, and P. A. Norreys, Phys. Rev. Lett. **98**, 125002 (2007).
[11] J. J. Santos *et al.*, Phys. Plasmas **14**, 103107 (2007); Phys. Rev. Lett. **89**, 025001 (2002).
[12] E. Brambrink *et al.*, Phys. Rev. E **75**, 065401(R) (2007).
[13] E. G. Gamaly, N. R. Madsen, M. Duering, A. V. Rode, V. Z. Kolev, and B. Luther-Davies, Phys. Rev. B **71**, 174405 (2005).
[14] Y. Zel'divich and Y. Raizer, *Physics of Shock Wave and High Temperature Phenomenae* (Academic Press, New York, London, 1966).
[15] R. More, K. Warren, D. Young, and G. Zimmerman, Phys. Fluids **31**, 3059 (1988).
[16] P. H. Maire, R. Abgral, J. Breil, and J. Ovadia, SIAM J. Sci. Comput. (USA) **29**, 1781 (2007).
[17] G. Schurtz *et al.*, Phys. Rev. Lett. **98**, 095002 (2007).
[18] C. Hirt, A. Amsden, and J. Cook, J. Comput. Phys. **135**, 203 (1997).
[19] K. Yasuike *et al.*, Rev. Sci. Instrum. **72**, 1236 (2001).
[20] O. Lundh, F. Lindau, A. Persson, C. G. Wahlstrom, P. McK-

enna, and D. Batani, Phys. Rev. E **76**, 026404 (2007).
[21] H. M. Milchberg, R. R. Freeman, S. C. Davey, and R. M. More, Phys. Rev. Lett. **61**, 2364 (1988).
[22] B. Chimier, V. T. Tikhonchuk, and L. Hallo, Phys. Rev. B **75**, 195124 (2007).
[23] R. B. Stephens *et al.*, Phys. Rev. E **69**, 066414 (2004).
[24] P. A. Norreys, J. Green, J. Davies, M. Tatarakis, E. Clark, F. Beg, A. Dangor, K. Lancaster, M. Wei, and K. Krushelnick, Plasma Phys. Controlled Fusion **48**, L11 (2006).